arXiv:1603.09043v2 [cond-mat.quant-gas] 10 Jun 2016

Rashba-type spin-orbit coupling in bilayer Bose-Einstein condensates

S.-W. Su,[1] S.-C. Gou,[1,2,*] Q. Sun,[3] L. Wen,[4] W.-M. Liu,[5] A.-C. Ji,[3,†] J. Ruseckas,[6] and G. Juzeliūnas[6,‡]

[1]*Department of Physics and Graduate Institute of Photonics, National Changhua University of Education, Changhua 50058, Taiwan*
[2]*National Center for Theoretical Sciences, Physics Division, Hsinchu 300, Taiwan*
[3]*Department of Physics, Capital Normal University, Beijing 100048, China*
[4]*College of Physics and Electronic Engineering, Chongqing Normal University, Chongqing, 401331, China*
[5]*Beijing National Laboratory for Condensed Matter Physics, Institute of Physics, Chinese Academy of Sciences, Beijing 100190, China*
[6]*Institute of Theoretical Physics and Astronomy, Vilnius University, Saulėtekio Ave. 3, Vilnius,10222, Lithuania*

(Dated: June 13, 2016)

We explore a way of producing the Rashba spin-orbit coupling (SOC) for ultracold atoms by using a two-component (spinor) atomic Bose-Einstein condensate (BEC) confined in a bilayer geometry. The SOC of the Rashba type is created if the atoms pick up a π phase after completing a cyclic transition between four combined spin-layer states composed of two spin and two layer states. The cyclic coupling of the spin-layer states is carried out by combining an intralayer Raman coupling and an interlayer laser assisted tunneling. We theoretically determine the ground-state phases of the spin-orbit-coupled BEC for various strengths of the atom-atom interaction and the laser-assisted coupling. It is shown that the bilayer scheme provides a diverse ground-state phase diagram. In an intermediate range of the atom-light coupling two interlacing lattices of half-skyrmions and half-antiskyrmions are spontaneously created. In the strong-coupling regime, where the SOC of the Rashba-type is formed, the ground state represents plane-wave or standing-wave phases depending on the interaction between the atoms. A variational analysis is shown to be in a good agreement with the numerical results.

PACS numbers: 67.85.-d, 05.30.Jp, 67.85.Fg, 64.60.My

I. INTRODUCTION

Following the first realization of artificial (synthetic) magnetic field for ultracold neutral atoms [1], quantum degenerate gases have provided a highly controllable test bed for studying the dynamics of quantum systems subjected to gauge potentials [2–5]. A possible way of creating synthetic gauge potentials for electrically neutral atoms relies on the adiabatic following of one of the atomic states "dressed" by the atom-light interaction [1, 6–11]. Such atoms can experience a light-induced Lorentz-like force, thus mimicking the dynamics of charged particles in a magnetic field [1, 8–12]. Likewise, non-Abelian gauge potentials can be created when a manifold of degenerate dressed states of atom-light interaction is involved [10–14].

An important implication of the synthetic non-Abelian gauge potentials is that they provide a coupling between the center-of-mass motion and the internal (spin or quasi-spin) degrees of freedom, forming an effective spin-orbit coupling (SOC). A variety of novel phenomena has been predicted for such systems, for example, the stripe phase and vortex structure in the ground states of spin-orbit-coupled Bose-Einstein condensates (BECs) [15–26], the Rashba pairing bound states (Rashbons) [27, 28] and topological superfluidity [29–31] in fermionic gases, as well as the superfluidity and Mott-insulating phases of spin-orbit-coupled quantum gases in optical lattice [32–36].

The synthetic SOC has been experimentally implemented for boson [37, 38] and fermion [39, 40] ultracold atomic gases by Raman coupling of a pair of atomic hyperfine ground states. This opens up possibilities of simulating exotic quantum matter featuring magnetic and spin–orbit effects for ultracold atoms. Despite an unprecedented controllability of ultracold atoms, the experimentally realized SOC [37–44] couples the atomic motion to its spin just in a single spatial direction. Such a one-dimensional (1D) SOC corresponds to an equally-weighted combination of the Rashba- and Dresselhaus-type of coupling [37, 45–47].

Realization of the synthetic SOC in two or more dimensions is highly desirable. The two dimensional spin-orbit coupling of the Rashba type has a non-trivial dispersion. It contains a Dirac cone at an intersection point of two dispersion branches, as well as a highly degenerate ground state (the Rashba ring), the latter leading to an unusual Bose-Einstein condensation [15–23, 25, 26]. Recently, a number of elaborate schemes has been suggested to create an effective two- and three-dimensional (2D and 3D) SOC [11, 48–58]. In particular, Campbell *et al*. proposed a way to generate the Rashba-type SOC by cyclically coupling N atomic internal states via the Raman transitions leading to a closed-loop (ring coupling) scheme [53].

A variant of such a scheme has been very recently experimentally implemented [59, 60] using a far detuned tripod setup corresponding to $N = 3$ in the ring coupling scheme [61]. A Dirac cone [59] and its opening [60] have been observed in the dispersion. However it does not seem realistic to observe the ground-state phases associated with the Rashba ring using the far detuning tripod setup which involves short-lived higher hyperfine ground states [59, 60]. Furthermore

* scgou@cc.ncue.edu.tw
† andrewjee@sina.com
‡ gediminas.juzeliunas@tfai.vu.lt

the $N = 3$ scheme used in the experiments [59, 60] converges slower to the Rashba ring than the $N = 4$ ring coupling scheme [53].

Recently Sun *et al* [58] put forward a scheme for generating a 2D SOC in a bilayer two-component BEC subjected to the Raman transitions and laser-assisted interlayer tunneling. In such a geometry the layer index provides an auxiliary degree of freedom to form a basis of four spin-layer states. It is noteworthy that the 2D SOC provided by such a bilayer setup does not represent the Rashba SOC [58]. Furthermore in such a setup the Raman transitions should be accompanied by a recoil in different directions for different layers, whereas the interlayer laser-assisted tunneling is to be accompanied by a recoil in different directions for different spin states [58]. These requirements would be extremely difficult to implement experimentally.

Here we consider an alternative bilayer scheme which is free from the above mentioned drawbacks and can provide a 2D SOC of the Rashba type. An essential element of the bilayer scheme is that the atoms now pick up a π phase after completing a cyclic transition between the four spin-layer states. In that case the dressed states of the atom-light coupling are two-fold degenerate. As a result, one effectively implements the $N = 4$ ring coupling scheme [53] by using a combination of two layers and two internal atomic states. If the interlayer tunneling and Raman transitions are sufficiently strong, the laser recoil induces a 2D SOC of the Rashba type for a pair of degenerate atomic dressed states. In that case the minimum of the single particle dispersion represents a degenerate Rashba-ring.

A characteristic feature of the bilayer system is that the interaction takes place between atoms belonging to the same layer. Therefore the atom-atom interaction is now different from the one featured for the scheme involving four cyclically coupled atomic internal states [53]. It is demonstrated that the bilayer scheme provides a diverse ground-state phase diagram. In particular, in the regime of a strong atom-light coupling the stripe and plane-wave phases emerge at specific directions of the degenerate Rashba-ring. Thus the system exhibits an interaction-induced anisotropy. On the other hand, in an intermediate range of the atom-light coupling, two interlacing lattices of half-skyrmions and half-antiskyrmions are formed.

The proposed bilayer setup can be experimentally implemented by using the current experimental technology. Unlike in the previous bilayer scheme [58], now the Raman coupling in each layer is accompanied by a recoil in the same direction $\mathbf{e}_x - \mathbf{e}_y$ in the xy plane, as one can see in Fig. 1. Consequently each layer is affected by the Raman coupling used previously to produce a 1D SOC [37]. The π phase shift can be realized if the Raman coupling has an out of plane momentum component k^z_Ω, such that the relative phase between the layers is $k^z_\Omega d_z = 2\varphi = \pi$, where d_z is an interlayer separation. On the other hand, the interlayer tunneling is accompanied by the recoil in the same direction $\mathbf{e}_x + \mathbf{e}_y$ in the xy plane for both spin states. Such an laser-assisted interlayer tunneling is also experimentally available [3, 4]. To implement the present bilayer setup one needs to combine the Raman coupling between the different spin states [37] together with the laser-assisted interlayer tunneling [3, 4]. An additional merit of the bilayer scheme is that only two atomic spin states are involved. Thus there is no need to make use of spin states belonging to a higher hyperfine manifold [53]. The latter spin states suffer from a collisional population decay [62] undermining the effective SOC.

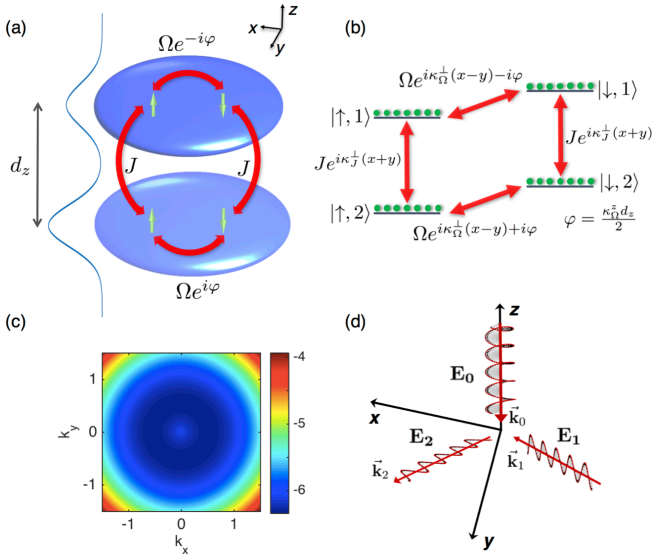

FIG. 1. (Color online) (a) Schematic plot of the atomic system. The BEC is tightly trapped in an asymmetric double-well potential along the z axis, forming a bilayer structure. The bosonic atoms in each layer are condensed into two single-particle internal states $|\gamma\rangle = |\uparrow\rangle, |\downarrow\rangle$. The layer index $j = 1, 2$ provides an extra degree of freedom, so the four states $|\gamma, j\rangle$ serve as the required atomic states in the $N = 4$ ring-coupling scheme [53]. The intralayer transitions, $|\uparrow, j\rangle \leftrightarrow |\downarrow, j\rangle$, are engendered by Raman coupling, while the interlayer transitions, $|\uparrow, 1\rangle \leftrightarrow |\uparrow, 2\rangle$ and $|\downarrow, 1\rangle \leftrightarrow |\downarrow, 2\rangle$ are due to the laser-assisted tunneling. (b) Schematic plot of the intralayer Raman transition and interlayer laser-assisted tunneling. (c) The lowest branch of the single-particle spectrum Eq. (6) for a strong symmetric coupling $\Omega = J = 5E_{\rm rec}$ and $\varphi = \pi/2$. The spectrum is plotted in units of recoil momentum κ and recoil energy $E_{\rm rec}$. In this case, a nearly degenerate Rashba-ring minimum with a radius $\kappa/2$ emerges. (d) A possible way to induce Raman transitions and interlayer tunneling by illuminating both layers with three laser beams, two of them $\mathbf{E}_1$ and $\mathbf{E}_2$ propagating in the xy plane, the third one $\mathbf{E}_0$ being along the z axis. The frequencies of the laser beams are chosen such that the $\mathbf{E}_0$ and $\mathbf{E}_1$ drive the Raman transition whereas $\mathbf{E}_0$ and $\mathbf{E}_2$ induces the laser-assisted interlayer tunneling. The field $\mathbf{E}_0$ provides the z component to the Raman coupling needed to have the phase difference 2φ for the Raman coupling in different layers. For more details see Appendix A.

The paper is organized as follows. In Sec. II, we construct the single-particle Hamiltonian describing spin-orbit-coupling in a bilayer BEC affected by the atom-light interaction. The single particle energy spectrum and corresponding eigenstates are determined for an arbitrary strength of atom-light coupling. In Sec. III, we consider the many-body ground-state phases of weakly interacting bilayer BECs by numerically solving the Gross-Pitaevskii equations in a wide range of mag-

nitudes of the interatomic interaction and the atom-light coupling. In the limit of strong atom-light coupling, we also analyze a behavior of the ground-state phase using a variational approach, and find it in a good agreement with the numerical results. In Sec. IV we present the concluding remarks and discuss possibilities of the experimental implementation of the proposed bilayer scheme. Finally some auxiliary calculations are placed in Appendixes A and B.

II. BILAYER BEC AFFECTED BY THE ATOM-LIGHT INTERACTION

A. Single-particle Hamiltonian

To realize the synthetic SOC in the atomic BEC based on the $N = 4$ close-loop (ring-coupling) scheme [53], we consider a two-component Bose gas confined in the bilayer geometry depicted in Fig. 1. The atoms are confined in a deep enough asymmetric double-well potential [63], so their motion is suppressed in the z-direction. The atoms are in the ground states of individual wells, and only the laser-assisted tunneling can induce transitions between the two wells. The four combined spin-layer states $|\gamma, j\rangle \equiv |\gamma\rangle_{\rm spin} \otimes |j\rangle_{\rm layer}$ serve as the states required for the ring coupling scheme [53]. Here $j = 1, 2$ signifies the j-th layer, and $|\gamma\rangle = |\uparrow\rangle, |\downarrow\rangle$ denotes an internal (quasi-spin) atomic state. The spin-layer states are cylindrically coupled by illuminating the atoms by three lasers inducing the intralayer Raman transitions and the laser-assisted interlayer tunneling, as depicted in Fig. 1. As it is shown in Appendix A, the resultant single-particle Hamiltonian can be represented as

$$\hat{H}_0 = \hat{H}_{\rm atom} + \hat{H}_{\rm intra} + \hat{H}_{\rm inter} + \hat{H}_{\rm extra}\,, \tag{1}$$

where

$$\hat{H}_{\rm atom} = \int d^2\mathbf{r}_\perp \sum_{j,\gamma} \hat{\psi}^\dagger_{\gamma j} \frac{\hbar^2 \mathbf{k}_\perp^2}{2m} \hat{\psi}_{\gamma j}\,, \tag{2}$$

is a Hamiltonian for an unperturbed atomic motion within the layers,

$$\hat{H}_{\rm intra} = \int d^2\mathbf{r}_\perp \Omega \left[e^{i\varphi} \hat{\psi}^\dagger_{\uparrow 1} \hat{\psi}_{\downarrow 1} + e^{-i\varphi} \hat{\psi}^\dagger_{\uparrow 2} \hat{\psi}_{\downarrow 2} + \text{H.c.} \right] \tag{3}$$

describes the spin-flip intralayer Raman transitions characterized by the Rabi frequency Ω, and

$$\hat{H}_{\rm inter} = \int d^2\mathbf{r}_\perp \sum_{\gamma} J \hat{\psi}^\dagger_{\gamma 2} \hat{\psi}_{\gamma 1} + \text{H.c.} \tag{4}$$

represents the laser-assisted interlayer tunneling with the strength J. Finally, the last term

$$\hat{H}_{\rm extra} = \int d^2\mathbf{r}_\perp \frac{\hbar^2 \kappa}{m} \left[\hat{\psi}^\dagger_{\uparrow 2} k_x \hat{\psi}_{\uparrow 2} - \hat{\psi}^\dagger_{\downarrow 1} k_x \hat{\psi}_{1\downarrow} + \hat{\psi}^\dagger_{\downarrow 2} k_y \hat{\psi}_{\downarrow 2} - \hat{\psi}^\dagger_{\uparrow 1} k_y \hat{\psi}_{\uparrow 1} \right], \tag{5}$$

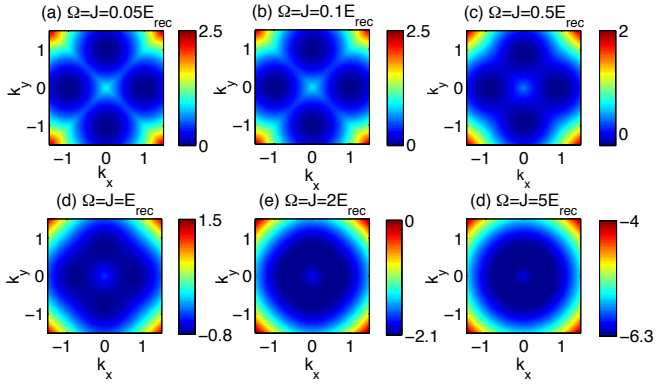

FIG. 2. (Color online) The lowest branch of the single-particle dispersion as a function of momentum for various coupling strengths are shown in (a)–(f). In a weak coupling regime $\Omega^2 = J^2 \ll E_{\rm rec}^2$, the dispersion is a superimposition of four distinct paraboloids centered at $\pm\kappa\hat{\mathbf{e}}_x$ and $\pm\kappa\hat{\mathbf{e}}_y$ as depicted in (a). Increasing the coupling strength, the four paraboloids become mixed with each other as plotted in (b) and (c) for $\Omega^2 = J^2 \lesssim E_{\rm rec}^2$ and the minima become much shallower as shown in (d) and (e) when $\Omega^2 = J^2 \sim E_{\rm rec}^2$. In the strong coupling regime $\Omega^2 = J^2 \gg E_{\rm rec}^2$ (see Ref. [53]), the Rashba-ring minimum with a radius $\kappa/2$ emerges, as one can see in (e) and (f).

describes the spin-orbit coupling due to the recoil momentum κ in the xy plane induced by the interlayer tunneling and Raman transitions. Here $\hat{\psi}_{\gamma j}$ is an operator annihilating an atom with a spin γ in the jth layer, $\mathbf{r}_\perp = (x, y)$ and $\mathbf{k}_\perp = \left(k_x, k_y\right)$ are in-plane projections of the atomic position vector and momentum, and $2\varphi = k^z_\Omega d_z$ is a phase difference between the Raman couplings in the two layers. The latter phase difference can be tuned by either varying the double-well separation d_z or the out-of-plane Raman recoil k^z_Ω. To implement an $N = 4$ ring coupling scheme with a π phase shift [53] the Raman coupling in different layers should have a π phase difference, so we set $\varphi = \pi/2$ throughout the paper.

Note that in the original representation the laser-induced terms $\hat{H}'_{\rm intra}$ and $\hat{H}'_{\rm inter}$ contain position dependent recoil factors featured in Eqs. (A2) and (A3) in Appendix A. Such a position-dependence can be eliminated via the transformation (A4) leading to a position-independent single-particle Hamiltonian $\hat{H}_0$ given by Eq. (1). Additionally, the spin-orbit coupling term $\hat{H}_{\rm extra}$ appears in the transformed Hamiltonian $\hat{H}_0$.

In the following, we shall work in dimensionless units where the energy is measured in units of the recoil energy $E_{\rm rec} = \hbar^2\kappa^2/2m$ and the wave-vector is measured in the units of κ.

B. Single-particle dispersion

Diagonalization of the single-particle Hamiltonian [Eq. (1)] yields four branches of the single-particle dispersion considered in Appendix B.1. Here, we focus only on the lowest branch characterized by the eigenenergies

$$E_g = 1 + k^2 - \sqrt{\Omega^2 + J^2 + 2k^2 + 2a_{\mathbf{k}}}\,, \tag{6}$$

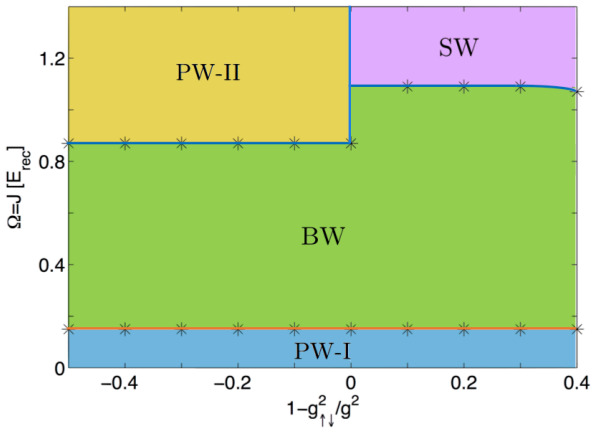

FIG. 3. (Color online) Ground-state phase diagram of the bilayer spin-orbit-coupled BEC as a function of $1 - g_{\uparrow\downarrow}^2/g^2$ and the laser-assisted coupling Ω for $J = \Omega$. The phase diagram consists of two types of plane-wave phases (PW-I: cyan and PW-II: yellow), a brick-wall phase (BW: green) and a standing-wave phase (SW: purple).

with

$$a_{\mathbf{k}} = \sqrt{\Omega^2(k_x + k_y)^2 + J^2(k_x - k_y)^2 + (k_x^2 - k_y^2)^2}\,, \qquad (7)$$

where $\mathbf{k} \equiv \mathbf{k}_\perp = \left(k_x, k_y\right)$ is an atomic momentum.

For a symmetric coupling ($\Omega = J$), the ground-state dispersion surface is plotted in Fig. 2 for various coupling strengths. In the following we shall present the corresponding eigenstates in different regimes of the coupling strength at the local minima of the dispersion surface where the atoms condense.

In the weak coupling regime, $\Omega^2 = J^2 \ll E_{\rm rec}^2$, the dispersion surface is built of superimposed paraboloids centered at $\pm\kappa\mathbf{e}_x$ and $\pm\kappa\mathbf{e}_y$, as shown in Fig. 2 (a). Each eigenstate corresponding to the four energy minima contains a single spin-layer component

$$|\downarrow,1\rangle e^{i\kappa x}\,, \quad |\uparrow,2\rangle e^{-i\kappa x}\,, \quad |\uparrow,1\rangle e^{i\kappa y}\,, \quad |\downarrow,2\rangle e^{-i\kappa y}\,, \qquad (8)$$

where

$$|\uparrow,1\rangle = \begin{pmatrix}1\\0\\0\\0\end{pmatrix}, \quad |\downarrow,1\rangle = \begin{pmatrix}0\\1\\0\\0\end{pmatrix}, \qquad (9)$$
$$|\uparrow,2\rangle = \begin{pmatrix}0\\0\\1\\0\end{pmatrix}, \quad |\downarrow,2\rangle = \begin{pmatrix}0\\0\\0\\1\end{pmatrix},$$

represents a basis of the spin-layer states. Therefore the four spin components are not yet mixed in the weak coupling limit.

With increasing the coupling to $\Omega^2 = J^2 \lesssim E_{\rm rec}^2$, the four paraboloids gradually coalesce but still the dispersion exhibits four distinguishable minima located at $\pm\kappa\mathbf{e}_x$ and $\pm\kappa\mathbf{e}_y$ as depicted in Figs. 2(b)–2(d). Each eigenstate corresponding to the four energy minima now contains contributions of three spin states

$$\begin{pmatrix}1\\\frac{2i}{\Omega}\\0\\-i\end{pmatrix}e^{i\kappa x}, \begin{pmatrix}1\\0\\\frac{-2}{J}\\i\end{pmatrix}e^{-i\kappa x}, \begin{pmatrix}\frac{-2i}{\Omega}\\1\\i\\0\end{pmatrix}e^{i\kappa y}, \begin{pmatrix}0\\1\\-i\\\frac{-2}{J}\end{pmatrix}e^{-i\kappa y}. \qquad (10)$$

This will lead to a brickwall phase for the bilayer BEC.

Finally in the strong coupling regime, $\Omega^2 = J^2 \gg E_{\rm rec}^2$, one has $a_{\mathbf{k}} \approx \Omega k\sqrt{2}$ and thus $E_g \approx -\Omega\sqrt{2} + 1 - k + k^2$. Hence mixing between the spin states results in the emergence of a cylindrically symmetric Rashba-ring minimum of a radius $\kappa/2$ in the dispersion shown in Fig. 2 (e) and (f). This is a characteristic feature of the close-loop (ring coupling) scheme [53]. In this regime, the single particle eigenstates $\Psi_{\mathbf{k}_g}$ on the Rashba-ring takes the form

$$\chi = \begin{pmatrix}\sqrt{2}\cos\phi\\ i(1-\sin\phi+\cos\phi)\\ 1-\sin\phi-\cos\phi\\ -\sqrt{2}i(1-\sin\phi)\end{pmatrix}\frac{e^{i\mathbf{k}\cdot\mathbf{r}_\perp}}{\sqrt{8-8\sin\phi}}\,, \qquad (11)$$

with $\mathbf{k} = \mathbf{k}_g = \kappa(\cos\phi\,\mathbf{e}_x + \sin\phi\,\mathbf{e}_y)/2$, where ϕ is an azimuthal angle parameterizing the degenerate ring.

It is convenient to project the system onto the state-vectors $\chi^{(1)}$ and $\chi^{(2)}$ corresponding to the spinor part of the ground-state-vector (11) for $\phi = 3\pi/4$ and $\phi = -\pi/4$, i.e. corresponding to the opposite momenta $\mathbf{k}$ and $-\mathbf{k}$ along the diagonal $\mathbf{e}_x - \mathbf{e}_y$, see Eq.(B13) in Appendix B.2. The projected Hamiltonian represents a Rashba-type Hamiltonian given by Eq.(B16).

Note that the Rashba-ring minimum occurs only for a symmetric coupling where $\Omega = J$. The asymmetric coupling ($\Omega \neq J$) breaks the rotational symmetry in the momentum space, reducing the ring minimum to a two-fold degenerate ground-state.

III. MEAN-FIELD GROUND STATES

A. Gross-Pitaevskii energy functional

We assume that all atoms interact with each other via contact potentials. As a result, the second-quantized interaction Hamiltonian is given by

$$\hat{H}_{\rm int} = \int d^2\mathbf{r}_\perp \sum_{j=1,2}\left(\frac{g_\uparrow}{2}\hat{n}_{\uparrow j}^2 + \frac{g_\downarrow}{2}\hat{n}_{\downarrow j}^2 + g_{\uparrow\downarrow}\hat{n}_{\uparrow j}\hat{n}_{\downarrow j}\right), \qquad (12)$$

where the interlayer interaction is neglected because of the short-range nature of the interatomic interactions. Here $g_\uparrow$ and $g_\downarrow$ denote the intraspecies interaction strengths, $g_{\uparrow\downarrow}$ is the interspecies interaction strength, and $\hat{n}_{\gamma j} = \hat{\psi}_{\gamma j}^\dagger\hat{\psi}_{\gamma j}$ is the number density operator for the γ-th spin state in the j-th layer. To approach the ground-state structure of the spin-orbit coupled BEC at zero temperature, we adopt the mean-field approximation, namely, the field operator, $\hat{\psi}_{\gamma j}$, is replaced by the ground-state expectation value, $\psi_{\gamma j} \equiv \langle\hat{\psi}_{\gamma j}\rangle$, which is complex in

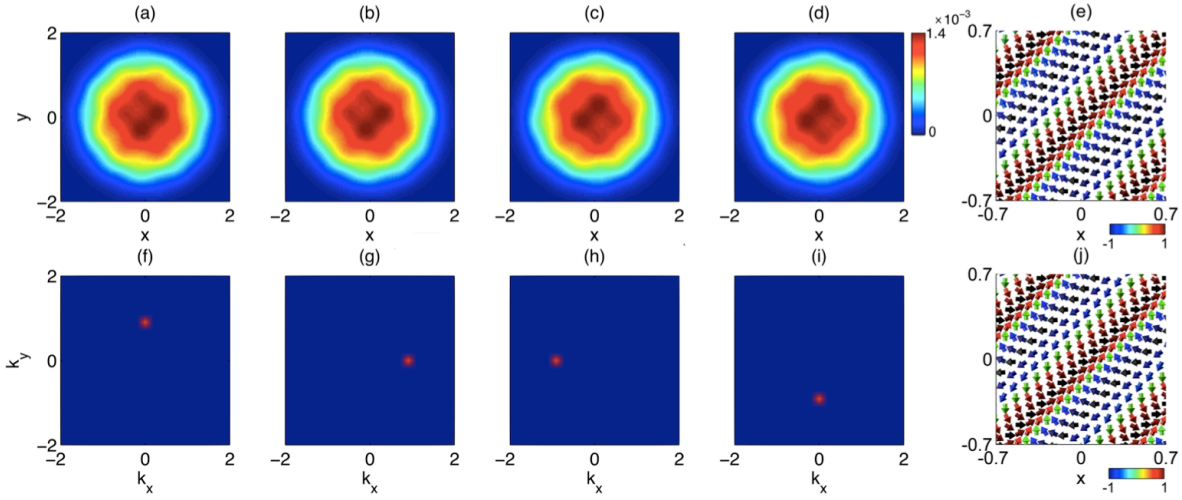

FIG. 4. (Color online) (a)–(d) Plots of the real-space density profiles of all spin-layer components for the PW-I phase, i.e., $\rho_{\uparrow 1}$, $\rho_{\downarrow 1}$, $\rho_{\uparrow 2}$, and $\rho_{\downarrow 2}$, respectively. The corresponding momentum-space distributions are depicted in (f)–(i), where the axes are in units of recoil momentum. The spin texture in the first and second layers are shown in (e) and (j), respectively, where the color of the arrows indicate the magnitude of S_j^x. The couplings and interaction strengths are taken to be $\Omega = J = 0.05E_{\rm rec}$ and $g_\uparrow : g_\downarrow : g_{\uparrow\downarrow} = 1 : 1 : 0.9$.

general. Accordingly, the Gross-Pitaevskii (GP) energy functional $\mathcal{E}[\psi^*_{\gamma j}, \psi_{\gamma j}] = \langle \hat{H}_0 + \hat{H}_{\rm int} \rangle$ is explicitly expressed as

$$\begin{aligned}\mathcal{E}[\psi^*_{\gamma j}, \psi_{\gamma j}] = \int d^2\mathbf{r}_\perp \Big[&\sum_{j,\gamma} \psi^*_{\gamma j}\Big(-\frac{1}{2}\nabla^2_\perp + \frac{1}{2}\omega^2 r^2\Big)\psi_{\gamma j} \\ &+ \kappa(\psi^*_{\uparrow 2}\hat{p}_x\psi_{\uparrow 2} - \psi^*_{\downarrow 1}\hat{p}_x\psi_{\downarrow 1}) \\ &+ \kappa(\psi^*_{\downarrow 2}\hat{p}_y\psi_{\downarrow 2} - \psi^*_{\uparrow 1}\hat{p}_y\psi_{\uparrow 1}) \\ &+ \Omega\left(e^{i\varphi}\psi^*_{\uparrow 1}\psi_{\downarrow 1} + e^{-i\varphi}\psi^*_{\uparrow 2}\psi_{\downarrow 2} + \text{H.c.}\right) \\ &+ J(\psi^*_{\uparrow 2}\psi_{\uparrow 1} + \psi^*_{\downarrow 2}\psi_{\downarrow 1} + \text{H.c.}) \\ &+ \sum_j \left(\frac{g_\uparrow}{2}\rho^2_{\uparrow j} + \frac{g_\downarrow}{2}\rho^2_{\downarrow j} + g_{\uparrow\downarrow}\rho_{\uparrow j}\rho_{\downarrow j}\right)\Big], \end{aligned} \tag{13}$$

where $\rho_{\gamma j} = |\psi_{\gamma j}|^2$, and the wave functions are normalized to the unity $\int d^2\mathbf{r}_\perp \sum_{j\gamma} \rho_{\gamma j}(\mathbf{r}_\perp) = 1$. This is achieved by the substitution $\psi_{\gamma j} \to \sqrt{N}\psi_{\gamma j}$ which rescales interaction strengths, viz., $g_{\uparrow\downarrow} \to Ng_{\uparrow\downarrow}$, $g_\uparrow \to Ng_\uparrow$ and $g_\downarrow \to Ng_\downarrow$, where N is the total number of atoms. Without loss of generality, we assume $g_\uparrow = g_\downarrow \equiv g$. Furthermore to confine atoms we have included a sufficiently weak harmonic trapping potential with a energy $\hbar\omega$ much smaller than the recoil energy $E_{\rm rec}$.

An important quantity characterizing the bilayer BEC is a spin texture on the j-th layer $\mathbf{S}_j(\mathbf{r}_\perp) = \langle \chi_j | \boldsymbol{\sigma} | \chi_j \rangle$ [64], where $\boldsymbol{\sigma} = \sigma_x\mathbf{e}_x + \sigma_y\mathbf{e}_y + \sigma_z\mathbf{e}_z$ is a vector of Pauli matrices, and $\chi_j(\mathbf{r}_\perp) = [\chi_{\uparrow j}(\mathbf{r}_\perp), \chi_{\downarrow j}(\mathbf{r}_\perp)]^T$ is a local spinor. The latter $\chi_j(\mathbf{r}_\perp)$ is proportional to the spinor wave-function $\psi_{\gamma j}(\mathbf{r}_\perp) = \sqrt{\sum_\gamma \rho_{\gamma j}(\mathbf{r}_\perp)}\chi_{\gamma j}(\mathbf{r}_\perp)$ and is normalized to unity $|\chi_{\uparrow j}|^2 + |\chi_{\downarrow j}|^2 = 1$. It is convenient to represent the spinor $\chi_j(\mathbf{r}_\perp)$ in terms of its amplitude and phase

$$\chi_{\gamma j}(\mathbf{r}_\perp) = |\chi_{\gamma j}| e^{i\theta_{\gamma j}}, \quad \text{with} \quad \gamma = \uparrow, \downarrow . \tag{14}$$

In that case the Cartesian components of the vector $\mathbf{S}_j$ take the form

$$\begin{aligned} S^x_j &= 2|\chi_{\uparrow j}||\chi_{\downarrow j}|\cos(\theta_{\downarrow j} - \theta_{\uparrow j}), \\ S^y_j &= 2|\chi_{\uparrow j}||\chi_{\downarrow j}|\sin(\theta_{\downarrow j} - \theta_{\uparrow j}), \\ S^z_j &= |\chi_{\uparrow j}|^2 - |\chi_{\downarrow j}|^2 . \end{aligned} \tag{15}$$

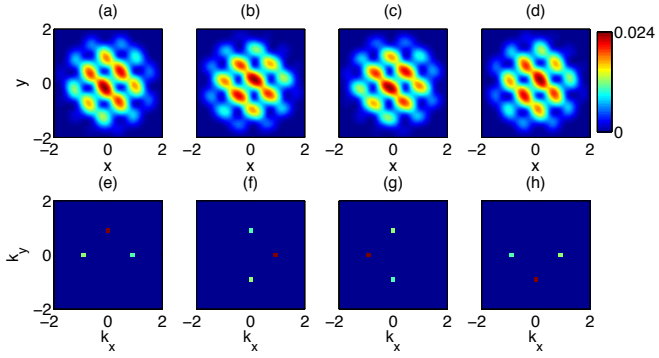

FIG. 5. (Color online) The real-space density profiles of all spin-layer components in BW phase, $\rho_{\uparrow 1}$, $\rho_{\downarrow 1}$, $\rho_{\uparrow 2}$ and $\rho_{\downarrow 2}$, are plotted in (a)-(d), respectively. The corresponding momentum-space distributions are depicted in (e)-(h), where the axes are calibrated in units of recoil momentum. The couplings and interaction strengths are taken to be $\Omega = J = 0.5E_{\rm rec}$ and $g_\uparrow : g_\downarrow : g_{\uparrow\downarrow} = 1 : 1 : 0.9$.

B. Numerical results

To investigate the ground-state phases of the interacting BEC in a harmonic trap, we minimize the GP energy functional Eq. (13) by the imaginary-time propagation method [65]. As shown in Fig. 3, the ground state possesses a variety of phases which are determined by the inter- and in-

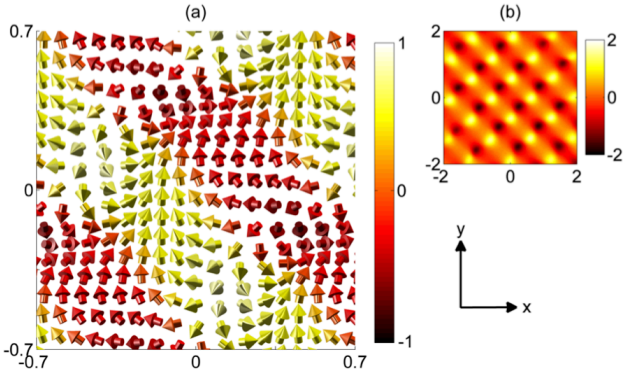

FIG. 6. (Color online) (a) Spin texture of the first layer for the BW phase depicted in Fig. 5. The color of the arrows indicates the magnitude of S_1^z. (b) The topological charge density of the spin orientation shown in (a). Two interlacing square lattices of positive and negative charges are clearly visible. Integrating the charge density over an unit cell for the lattice of positive (negative) charge gives $1/2$ $(-1/2)$ which corresponds to the half-skyrmion (half-antiskyrmion).

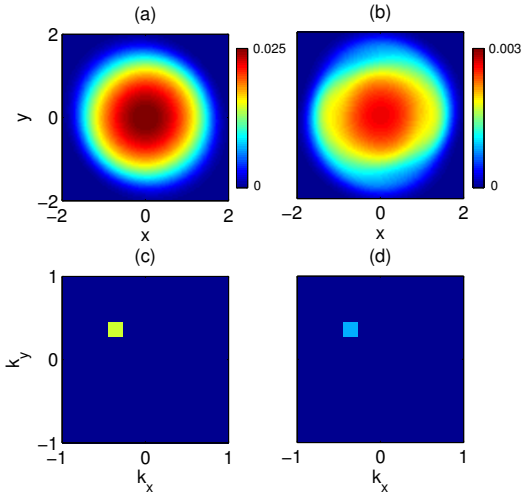

FIG. 7. (Color online) (a) and (b) The real-space density profiles of the spin-layer components $\rho_{\uparrow 1}$ and $\rho_{\downarrow 1}$ in the first layer for PW-II phase with $\mathbf{k} = \kappa \mathbf{e}_-/2$. The corresponding momentum-space distributions are depicted in (c) and (d), where the axes are marked in units of the recoil momentum. The couplings and interaction strengths are taken to be $\Omega = J = 2E_{\rm rec}$ and $g_\uparrow : g_\downarrow : g_{\uparrow\downarrow} = 1 : 1 : 1.1$.

tralayer coupling and the intralayer interaction between the atoms. In the numerical simulations, four distinct phases have been identified. These are the plane-wave phases of types I and II (PW-I and PW-II), the brick-wall (BW) phase, as well as the standing-wave (SW) or stripe phase. The occurrence of PW-I and BW phases depends only on the Raman coupling and the interlayer tunneling. On the other hand, the PW-II and SW phases emerge at stronger Raman coupling and stronger tunneling, and depend on the interatomic interactions. In the following, the structure of each phases is discussed.

PW-I phase. In a weak coupling regime, $\Omega^2 = J^2 \ll E_{\rm rec}^2$, the four spin-layer components are almost uncoupled. Consequently each layer behaves like an ordinary binary BEC except that the single-particle dispersion is shifted due to the term $\hat{H}_{\rm extra}$, Eq. (5), induced by the gauge-transformation (A4). Therefore, each spin-layer component would condense at the bottom of the shifted parabolic dispersion, as shown in Fig. 4. The real-space density profiles of the four spin-layer components, $|\psi_{\gamma j}(\mathbf{r}_\perp)|^2$, are presented in Fig. 4 (a)–(d), and their momentum-space counterparts, $|\bar{\psi}_{\gamma j}(\mathbf{k})|^2$, are shown in Fig. 4 (f)–(i). The momentum distribution of each component, $|\bar{\psi}_{\gamma j}(\mathbf{k})|^2$, is sharply peaked around the four momenta, $\mathbf{k} = \kappa \mathbf{e}_x$, $-\kappa \mathbf{e}_x$, $\kappa \mathbf{e}_y$ and $-\kappa \mathbf{e}_y$, indicating that each spin-layer component acquires a momentum shift via the SOC term $\hat{H}_{\rm extra}$ given by Eq. (5).

The spin texture $\mathbf{S}_j(\mathbf{r}_\perp)$ of PW-I phase is depicted in Figs. 4(e) and 4(j) for the first layer ($j = 1$). The color of the arrows indicates the magnitude of S_j^x and the periodic modulation of spin orientation is caused by the interference between the plane waves characterizing the spin-layer components.

BW phase. By simultaneously increasing Ω and J, the four otherwise distinct paraboloids characterizing the PW-I phase start developing a noticeable overlap between the neighboring paraboloids and finally completely merge in the moderate coupling regime where $\Omega^2 = J^2 \lesssim E_{\rm rec}^2$. The dispersion surface so formed introduces a ground-state phase shown in Figs. 5(a)-5(d). The BEC density profiles of the four spin-layer components now exhibit periodic spatial modulations characteristic to a BW pattern. Note that the dips in the density profiles are not vortices according to their phase profiles. The BW patterns of both spin components in the same layer interlace, so that the density dips of one spin component are filled by another spin component. The formation of BW structure can be easily understood by examining the density profiles in the momentum space.

As shown in Figs. 5(e)-5(h), it is evident that $\bar{\psi}_{\gamma j}(\mathbf{k})$ appears as a superposition of three out the four-momentum eigenmodes labeled by $\mathbf{k} = \pm\kappa \mathbf{e}_x$ and $\pm\kappa \mathbf{e}_y$. For instance, let us take $\psi_{\uparrow 1}$ representing a superposition of the modes with $\mathbf{k} = \pm\kappa \mathbf{e}_x$ and $\kappa \mathbf{e}_y$. In this case the majority of atoms condense in the $\mathbf{k} = \kappa \mathbf{e}_y$ mode, whereas the remaining atoms evenly condense in the $\mathbf{k} = \pm\kappa \mathbf{e}_x$ modes. The latter two modes are populated owing to the presence of non-negligible inter- and intralayer couplings.

In contrast to the PW-I phase, the BW structure leads to an intriguing spin texture in each layer, as shown in Fig. 6. The spin texture consists of two interlacing square lattices of spin vortices with opposite handednesss. To further characterize this state, we calculate the topological charge density in the j-th layer, $\tau_j = \mathbf{S}_j \cdot \partial_x \mathbf{S}_j \times \partial_y \mathbf{S}_j / 4\pi$. As shown in Fig. 6, the left (right)-handed circulation corresponds to a positive (negative) topological charge density. Integrating τ_j over the elementary unit cell, we identify that the topological charge can be either $+1/2$ or $-1/2$. This corresponds to the half-skyrmions and half-antiskyrmions, respectively [54, 58, 66, 67].

PW-II phase. Now let us assume that $g_{\uparrow\downarrow} > g$ and consider the strong coupling limit where $\Omega^2 = J^2 \gg E_{\rm rec}^2$. In this regime, the Rashba-ring minimum emerges, and the many-body ground state (PW-II phase) becomes interaction-dependent. Figure 7 illustrates formation of the PW-II phase

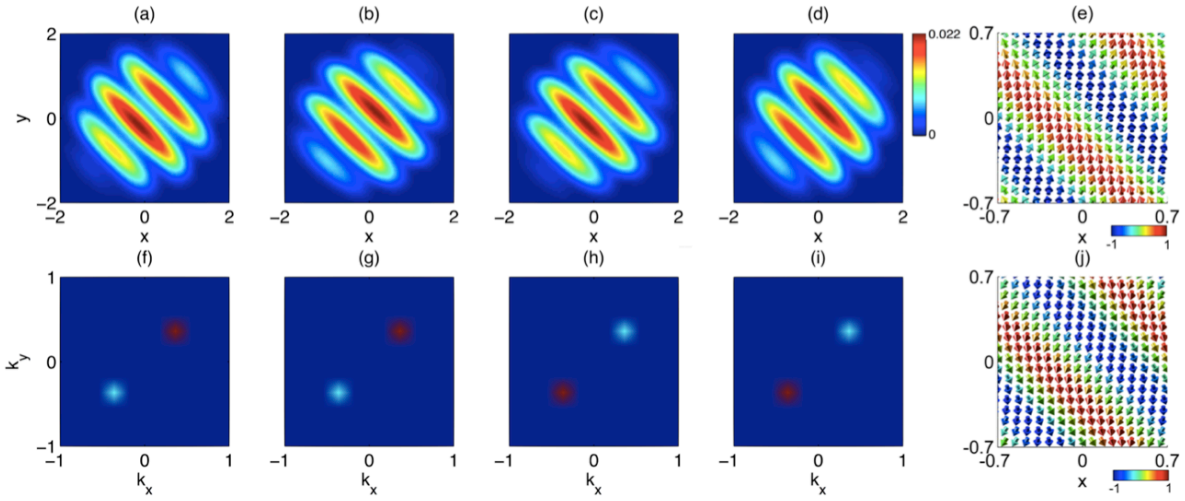

FIG. 8. (Color online) The real-space density profiles of all spin-layer components in SW phase, $\rho_{\uparrow 1}$, $\rho_{\downarrow 1}$, $\rho_{\uparrow 2}$ and $\rho_{\downarrow 2}$, are plotted in (a)–(d), respectively. The corresponding momentum-space distributions are depicted in (f)–(i), where the axes are calibrated in units of recoil momentum. The spin texture in the first and second layers are shown in (e) and (j), respectively where the color of the arrows indicate the magnitude of S^z_j. The couplings and interaction strengths are taken to be $\Omega = J = 2E_{\rm rec}$ and $g_\uparrow : g_\downarrow : g_{\uparrow\downarrow} = 1 : 1 : 0.9$.

for $\Omega = J = 2E_{\rm rec}$ and $g_\uparrow : g_\downarrow : g_{\uparrow\downarrow} = 1 : 1 : 1.1$ corresponding to the case where $g_{\uparrow\downarrow} > g$. Unlike in the PW-I phase, here each spin-layer component condenses in the same momentum mode with $\mathbf{k} = \pm\kappa\mathbf{e}_-/2$ along the diagonal $\mathbf{e}_- = (\mathbf{e}_x - \mathbf{e}_y)/\sqrt{2}$, and the total multicomponent wave function contains a common plane-wave factor. In each layer the intralayer spin polarization is non-zero due to the imbalanced population of $\rho_{\uparrow j}$ and $\rho_{\downarrow j}$. On the other hand, the density profiles of the same spin-component but different layers are identical, i.e., $\rho_{\gamma 1} = \rho_{\gamma 2}$. Note that in the previously considered Rashba-type SO-coupled system [15], the plane wave phase exists in the regime where $g_{\uparrow\downarrow} < g$. This is opposite to the current bilayer system.

SW phase.– Finally, for $g_{\uparrow\downarrow} < g$ and $\Omega^2 = J^2 \gg E_{\rm rec}^2$, the ground-state wave function consists of two counterpropagating plane-waves on the Rashba ring with opposite momenta along the diagonal $\mathbf{e}_+ = (\mathbf{e}_x + \mathbf{e}_y)/\sqrt{2}$. This constitutes the SW phase. As shown in Fig. 8, the real-space density profile of each component with $\Omega = J = 2E_{\rm rec}$ and $g_\uparrow : g_\downarrow : g_{\uparrow\downarrow} = 1 : 1 : 0.9$ forms the stripe structure, while the momentum-space density is sharply peaked around the of two momenta $\mathbf{k} = \pm\kappa\mathbf{e}_+/2$. The spin texture in each layer is depicted in Figs. 8(e) and 8(j). The periodic modulation of the spin texture is accompanied by the stripe structure of the density profile. Furthermore, one can see in Fig. 8 that the occupation of the two momentum states $\mathbf{k} = (\pm\kappa/2)\mathbf{e}_+$ is asymmetric in the bilayer system, in contrast to the SW phase in the previously considered SO-coupled BECs [15, 20–22, 24, 26]. It is noteworthy that now the SW phase occurs for $g_{\uparrow\downarrow} < g$. This is opposite to the usual BEC affected by the Rashba SOC [15]. To further understand the the phases of the bilayer system, a variational analysis is presented in the following section.

C. Variational approach

So far our conclusions on the BEC phases were based mostly based on numerical simulations. In order to gain a better insight into the ground-state structure of the bilayer SO-coupled BEC, a simpler analytical study is desirable. To this end, we employ a variational approach to investigate the ground-state phases in different coupling regimes. We are particularly interested in solving the ground-state in the strong-coupling regime, where the many-body ground state shows a preference of residing at some special locations of the degenerate Rashba ring.

We begin by writing down the interaction energy, namely, the ground-state expectation value of the interaction Hamiltonian (16)

$$\mathcal{E}_{\rm int} = \frac{1}{4}\sum_j \left(c_0\rho_j^2 + c_2\mu_j^2\right), \tag{16}$$

where $\rho_j = \rho_{\uparrow j} + \rho_{\downarrow j}$ and $\mu_j = \rho_{\uparrow j} - \rho_{\downarrow j}$ are respectively the total number and magnetization densities in the j-th layer, and $c_0 = g + g_{\uparrow\downarrow}$ and $c_2 = g - g_{\uparrow\downarrow}$ characterize the density-density and spin-spin interactions, respectively. We use the following trial wave functions of PW-II and SW phases

$$\Psi^{\rm PW-II} = \Psi_{\mathbf{k}_g} \tag{17}$$

and

$$\Psi^{\rm SW} = \frac{1}{\sqrt{2}}(\Psi_{\mathbf{k}_g} + \Psi_{-\mathbf{k}_g}), \tag{18}$$

where $\Psi_{\mathbf{k}_g}$ is the plane-wave solution given by Eq. (11), with $\mathbf{k}_g = \kappa(\cos\phi\,\mathbf{e}_x + \sin\phi\,\mathbf{e}_y)/2$. In the following, we compare the interaction energies for these two trial wave functions. For simplicity, we shall not include a harmonic trapping potential.

PW-II phase. Let us first consider the variational ansatz of PW-II phase. With the trial wave function given by Eq. (17), the total density and spin density in the j-th layer read

$$\rho_j = \frac{1}{2} + \frac{(-1)^{j-1}(\cos\phi + \sin\phi)}{4} \tag{19}$$

and

$$\mu_j = \frac{\sin\phi - \cos\phi}{4}\,. \tag{20}$$

Therefore, for the PW-II phase the nonlinear interaction energy is given by

$$\mathcal{E}_{\rm int}^{\rm PW-II} = \frac{c_0}{8} + \frac{c_0}{64}(1+\sin 2\phi) + \frac{c_2}{32}(1-\sin 2\phi)\,. \tag{21}$$

It is evident that the interaction energy depends on the azimuthal angle ϕ. This is in contrast to the single-layer Rashba SO-coupled system in which the interaction energy does not depend on the azimuthal angle ϕ [15, 20, 24]. Using Eq. (21), the energy minima are found at two angles $\phi = 3\pi/4$ and $-\pi/4$, for which

$$\mathcal{E}_{\rm int,\,min}^{\rm PW-II} = \frac{c_0}{8} + \frac{c_2}{16}\,. \tag{22}$$

SW phase. For the SW phase, the trial wave function Eq. (18) provides the following total density and magnetization density:

$$\rho_j = \frac{1}{2} + \frac{1}{4}|\cos\phi|(\tan\phi - 1)\cos(x\cos\phi + y\sin\phi) \tag{23}$$

and

$$\mu_j = \frac{1}{4}|\cos\phi|(1+\tan\phi)\cos(x\cos\phi + y\sin\phi), \tag{24}$$

where the spatial dependence comes from the periodic modulation of the stripes. The resultant energy takes the form

$$\mathcal{E}_{\rm int}^{\rm SW} = \frac{c_0}{8} + \frac{c_0}{64}(1-\sin 2\phi) + \frac{c_2}{64}(1+\sin 2\phi), \tag{25}$$

where the spatially oscillating cosine terms are replaced by the mean values $\langle\cos(x\cos\phi + y\sin\phi)\rangle = 0$ and $\langle\cos^2(x\cos\phi + y\sin\phi)\rangle = 1/2$. Thus the interaction is again anisotropic along the Rashba ring. The energy minimum occurs at $\phi = \pi/4$ or equivalently at $5\pi/4$

$$\mathcal{E}_{\rm int,\,min}^{\rm SW} = \frac{c_0}{8} + \frac{c_2}{32}. \tag{26}$$

The energy minima of the PW-II and SW phases differ by the amount $\mathcal{E}_{\rm int,\,min}^{\rm PW-II} - \mathcal{E}_{\rm int,\,min}^{\rm SW} = c_2/32$. This implies that for $c_2 > 0$ ($c_2 < 0$) the SW (PW-II) phase represents the ground state, in agreement with the numerical simulations. Although the ordinary single layer Rashba SOC also provides the SW and PW-II phases [15], the conclusions are opposite compared to our bilayer system, that is, for $c_2 < 0$ ($c_2 > 0$) the ground state is in the SW (PW-II) phase.

We note that in a single-layer Rashba SOC the energy of the PW phase is spin-independent on a Rashba ring, and the phase has a zero magnetization [15]. On the other hand, in the bilayer system the energy minima of PW-II phase on the Rashba ring are characterized by a non-vanishing magnetization. Therefore the PW-II phase has a lower energy than the SW phase for $c_2 < 0$ corresponding to $g_{\uparrow\downarrow} > g$. In this way one arrives at a situation opposite to that appearing for an ordinary single layer BEC affected by the SOC [15] in which the PW phase has an energy lower than the SW phase if $c_2 > 0$ corresponding to $g_{\uparrow\downarrow} > g$. The difference originates from the anisotropy in the population of each spin-layer component on the Rashba ring in the bilayer system, as one can see in Eq. (11).

In this way, the variational approach shows that the atoms favor to condense at $\phi = 3\pi/4$ or $-\pi/4$ for the PW-II phase, whereas the SW phase involves a superposition of the plane waves at $\phi = \pi/4$ and $5\pi/4$. To gain more insight into such an interaction-induced symmetry breaking, in the Appendix B.3 the Hamiltonian has been expressed in terms of the basis vectors of the lowest dispersion branch at the azimuthal angles $\phi = 3\pi/4$ or $-\pi/4$. The projection of the Hamiltonian onto these states gives rise to the appearance of the Rashba Hamiltonian (B16) subjected to an asymmetric atom-atom interaction given by Eq.(B19).

We have presented the variational study in the regime of strong coupling. For a weak and a moderate coupling, the single-particle dispersion surfaces are characterized by four distinct minima in the momentum space. The trial wave functions are then simply superpositions of the four corresponding momentum eigenstates. This provides the ground state phases in a good agreement with the numerical results.

Asymmetric coupling $\Omega \neq J$

Now let us briefly discuss a situation when $\Omega \neq J$ and $\sqrt{\Omega^2 + J^2} \gg E_{\rm rec}$. The asymmetric coupling breaks the rotational symmetry in the momentum space and leads to a two-fold degenerate single-particle dispersion. For $\Omega > J$, the energy minimum occurs at $\phi = \pi/4$ and $5\pi/4$, while for $\Omega < J$, the energy minimum appears at $\phi = -\pi/4$ and $3\pi/4$. Numerical simulations reveal that the many-body ground state is the SW or PW-II phase for $\Omega > J$ or $\Omega < J$, respectively. The phase is independent of the interaction strengths. This is because the single particle dispersion possesses only two degenerate minima. In other words, due to the lack of the ring degeneracy, the many-body ground state is determined only by the strengths of the Raman coupling and the tunneling.

Metastable states

Occasionally the imaginary-time propagation ended up at a metastable state containing domains. The metastable state emerges for parameters of the system corresponding to the PW-II phase, namely, for $c_2 < 0$ with $\Omega^2 = J^2 \gg E_{\rm rec}^2$ or for $\Omega \neq J$ with $\sqrt{\Omega^2 + J^2} \gg E_{\rm rec}$. It has an energy slightly higher than that of the ground state. The metastable state is made of two spatially separated spin-polarized domains in the same layer, as shown in Fig. 9. The domains carry opposite

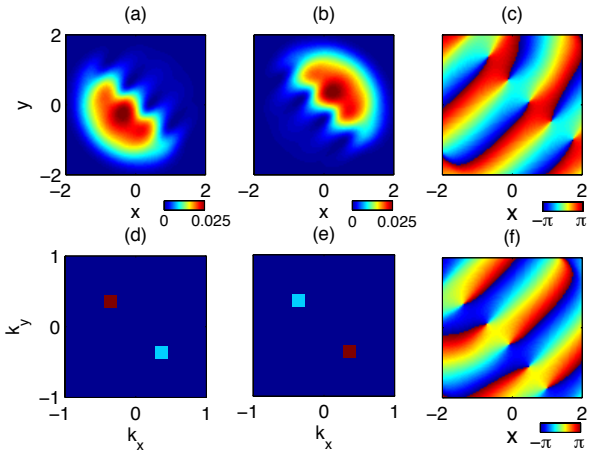

FIG. 9. (Color online) The real-space density profiles of spin components in the first layer in a metastable state, $\rho_{\uparrow 1}$ are $\rho_{\downarrow 1}$, are plotted in (a)–(b), respectively. The corresponding momentum-space distributions are depicted in (d)–(e), where the axes are calibrated in units of recoil momentum. The coupling is now asymmetric, $\Omega = 1.5E_{rec}$ and $J = 2E_{rec}$, and interaction strengths are $g_\uparrow : g_\downarrow : g_{\uparrow\downarrow} = 1 : 1 : 0.9$. The phase profiles of the wave function in the first layer, $\theta_{\uparrow 1}(\mathbf{r})$ and $\theta_{\downarrow 1}(\mathbf{r})$ are plotted in (c) and (f), respectively, where an array of vortices can be clearly seen.

momenta, $\mathbf{k} = \pm\kappa\mathbf{e}_-/2$, like in the previously considered case of the ordinary Rashba SOC [15]. Since the phases of the two counterpropagating PW-II states in each domain could not continuously connect along the boundary, the frustration results in the formation of arrays of vortices, as depicted in Figs. 9(c) and 9(f). The density of the vortices increases with increasing the SOC strength.

IV. DISCUSSION AND CONCLUSION

In conclusion, the proposed bilayer system provides a possibility to realize the Rashba-type SOC for ultracold atoms. Numerical simulation and variational analysis have elucidated a diverse phase diagram of the bilayer BEC in a wide range of magnitudes of the atom-light coupling and atom-atom interaction. In the moderate coupling regime the BW phase is formed leading to the emergence of lattices of half-skyrmions and half-antiskyrmions. In the strong coupling regime, the Rashba-ring minimum emerges, and the ground state is either the SW or PW-II phases, depending on the interatomic interaction strengths.

An experimental implementation of the proposed bilayer SO-coupled system is within reach of current experiments with ultracold atoms. For instance, the two magnetic sublevels of the $F = 1$ ground state manifold of the ^{87}Rb-type alkali atoms [37] could serve as the atomic internal (quasi-spin 1/2) states. Typically the experimental trapping frequencies are $(\omega_\perp, \omega_z) = 2\pi \times (10, 400)$ Hz and the wavelength of laser fields inducing the Raman coupling and interlayer tunneling is around $\lambda_L \simeq 800$ nm, corresponding to the recoil energy $E_{\rm rec} \simeq 11\hbar\omega_\perp$. The scattering lengths for the two spin states $|F = 1, m_F = 0\rangle \equiv |\uparrow\rangle$ and $|F = 1, m_F = -1\rangle \equiv |\downarrow\rangle$, used in Ref. [37], are given by $a_\uparrow = c_0$ and $a_\downarrow = a_{\uparrow\downarrow} = c_0 + c_2$, with $c_0 = 7.79 \times 10^{-12}\,\mathrm{Hz\,cm^3}$ and $c_2 = -3.61 \times 10^{-14}\,\mathrm{Hz\,cm^3}$ [68, 69]. The intra and interspecies interaction strengths are given by $g_{\uparrow,\downarrow} = \sqrt{2\pi}Na_{\uparrow,\downarrow}/\xi_z$ and $g_{\uparrow\downarrow} = \sqrt{2\pi}Na_{\uparrow\downarrow}/\xi_z$ with $\xi_z = \sqrt{\hbar/m\omega_z}$. The corresponding intra-species interaction is nearly symmetric with $g_\uparrow/g_\downarrow = 1.0047$, so the phase diagram of Fig. 3 can be applied directly. Finally, the diverse phase diagram of the bilayer system also provides the possibilities to study the quantum phase transition by varying the coupling strengths which will be investigated in another study.

ACKNOWLEDGMENTS

SWS and SCG are supported by Ministry of Science and Technology, Taiwan (Grants No. MOST 103-2112- M-018- 002-MY3). SCG is also supported by National Center for Theoretical Sciences, Taiwan. WML is supported by NSFC (Grants Nos. 11434015, 61227902, 61378017), by NKBRSFC (Grants Nos. 2011CB921502, 2012CB821305), by SKLQOQOD (Grants No. KF201403), and by SPRPCAS (Grants No. XDB01020300). GJ is supported by Lithuanian Research Council (Grants No. MIP-086/2015). ACJ and QS are supported by NSFC (Grants No. 11404225 and No. 11474205). LW is supported by NSFC (Grants Nos. 11504037).

Appendix A: Atom-Light Interaction

In this Appendix, we provide a full account of the atom-light interaction processes proposed for generating SOC in a bilayer BEC. The general Hamiltonian $H_{\rm AL}$ of the atom-light interaction in an atomic hyperfine ground-state manifold is expressed in terms of the scalar and vector light shifts [11, 70]:

$$H_{\rm AL} = u_s(\mathbf{E}^* \cdot \mathbf{E}) + \frac{iu_v g_F}{\hbar g_J}(\mathbf{E}^* \times \mathbf{E}) \cdot \hat{\mathbf{F}}, \qquad \text{(A1)}$$

where $\mathbf{E}^*$ is negative frequency part of the full electric field, $\hat{\mathbf{F}}$ the total spin operator, and u_s and u_v are the scalar and vector atomic polarizabilities. The parameters g_J and g_F denote the Land g-factors due to the electronic spin and the total angular momentum of the atom, respectively. For ^{87}Rb atoms in the lowest energy hyperfine manifold with $F = 1$, one has $g_F/g_J = -1/4$. Additionally, the atoms are trapped in a spin-independent asymmetric double-well potential [63]. The energy difference for the atomic ground states localized in different layers is $\Delta_{\rm inter}$, whereas the Zeeman splitting between atomic internal spin states within a layer is $\Delta_{\rm intra}$.

Figure 1 (d) illustrates the laser configuration for creating the desirable intra- and interlayer couplings. As shown in Fig. 1 (a), both layers are simultaneously illuminated by three laser beams labeled by $\mathbf{E}_0$, $\mathbf{E}_1$, and $\mathbf{E}_2$. The former field $\mathbf{E}_0 \sim (\mathbf{e}_x + i\mathbf{e}_y)e^{i(k_0 z - \omega_0 t)}$ is circularly polarized and propagates along the z-axis. It contributes both to the intra- and interlayers coupling. The latter fields $\mathbf{E}_1$ and $\mathbf{E}_2$ are responsible

for producing the intra- and interlayer couplings, respectively. In the following we shall consider these couplings in more details.

1. Intralayer transitions

The other applied field, $\mathbf{E}_1 \sim \hat{\mathbf{e}}_z e^{i[\mathbf{k}_1\cdot\mathbf{r}-(\omega_0+\delta\omega_1)t]}$, is linearly polarized along $\hat{\mathbf{e}}_z$ and is characterized by the wave vector $\mathbf{k}_1 = k_1\mathbf{e}_-$ in the xy-plane, as one can see in Fig. 1 (d), where $\mathbf{e}_- = (\mathbf{e}_x - \mathbf{e}_y)/\sqrt{2}$. The vector product $\mathbf{E}_0^* \times \mathbf{E}_1$ in Eq. (A1) describes the intralayer spin-flip transitions taking place if the frequencies of the fields $\mathbf{E}_0$ and $\mathbf{E}_1$ are tuned to the two-photon resonance, $\delta\omega_1 = \Delta_{\text{intra}}$, between the magnetic sublevels $|\downarrow\rangle \equiv |m_F = -1\rangle$ and $|\uparrow\rangle \equiv |m_F = 0\rangle$. The third magnetic sublevel $|m_F = 1\rangle$ can be excluded due to a sufficiently large quadratic Zeeman effect, as demonstrated by the NIST group [37]. Therefore, the Hamiltonian of the intralayer Raman coupling can be written as

$$\hat{H}'_{\text{intra}} = \int d^2\mathbf{r}_\perp \sum_j [\Omega e^{i(\mathbf{k}_\Omega^\perp\cdot\mathbf{r}_\perp + (-1)^j\varphi - \delta\omega_1 t)} + \text{c.c.}] \times \hat{\Phi}^\dagger_{\uparrow j}\hat{\Phi}_{\downarrow j} + \text{H.c.}\,, \tag{A2}$$

where $\mathbf{k}_\Omega = \mathbf{k}_1 - \mathbf{k}_0 = k_\Omega^\perp\mathbf{e}_- + k_\Omega^z\mathbf{e}_z$ with $k_\Omega^\perp = k_1$ and $k_\Omega^z = k_0$. Here $\hat{\Phi}_{\gamma j}(\mathbf{r}_\perp, z)$ is a field operator annihilating an atom in the spin-layer state $|\gamma, j\rangle$, and Ω is the Rabi frequency of the intralayer Raman coupling. Since the atoms move freely only the xy plane, the out-of-plane Raman recoil provides the phase difference $2\varphi = k_\Omega^z d_z$ for the Raman coupling in different layers. The phase difference can be tuned by either varying the double-well separation d_z or the out-of-plane Raman recoil k_Ω^z. In what follows, we take $\varphi = \pi/2$ to get the $N = 4$ close-loop scheme [53].

2. Interlayer tunneling

The third applied field, $\mathbf{E}_2 \sim \mathbf{e}_- e^{i[\mathbf{k}_2\cdot\mathbf{r}-(\omega_0+\delta\omega_2)t]}$, propagates along $\mathbf{k}_2 = k_2\mathbf{e}_+$ with $\mathbf{e}_+ = (\mathbf{e}_x + \mathbf{e}_y)/\sqrt{2}$ and is linearly polarized along $\mathbf{e}_-$ in the xy-plane. Since $\mathbf{E}_0$ and $\mathbf{E}_2$ are not orthogonal, their scalar product $\mathbf{E}_0\cdot\mathbf{E}_2$ featured in Eq. (A1), provides a scalar light shift oscillating with a frequency $\delta\omega_2$. This gives rise to the *state-independent* inter-layer transitions depicted in Fig. 1(c). To drive the such transitions, the frequencies of laser beams are assumed to satisfy the condition of two-photon interlayer resonance, $\delta\omega_2 = \Delta_{\text{inter}}$. The resultant Hamiltonian for the laser-assisted tunneling takes the form

$$\hat{H}'_{\text{inter}} = \int d^2\mathbf{r}_\perp \sum_\gamma \left(J e^{i\mathbf{k}_J^\perp\cdot\mathbf{r}_\perp - i\delta\omega_2 t} + \text{c.c.}\right)\hat{\Phi}^\dagger_{\gamma 2}\hat{\Phi}_{\gamma 1} + \text{H.c.}\,, \tag{A3}$$

where $\mathbf{k}_J = \mathbf{k}_2 - \mathbf{k}_0 = k_J^\perp\mathbf{e}_+ + k_J^z\mathbf{e}_z$ with $k_J^\perp = k_2$ and $k_J^z = k_0$. Here $J = \Omega_J\int dz\phi_2^*(z)\phi_1(z)e^{ik_J^z z}$ is the inter-layer coupling with Ω_J being the corresponding Rabi frequency, whereas $\phi_{1,2}(z)$ are the Wannier-like states localized at the layer 1 or 2. Note that the Wannier-like states $\phi_1(z)$ and $\phi_2(z)$ are orthogonal. Therefore the non-vanishing overlap integral determining J comes from the contribution of the factor $e^{ik_J^z z} \equiv e^{ik_0 z}$ due to the momentum transfer along the tunneling direction $\mathbf{e}_z$ [4]. Since the length of the in-plane wave-vectors $\mathbf{k}_1$ and $\mathbf{k}_2$ is almost the same, in the following we shall take $k_J^\perp = k_\Omega^\perp = \kappa$.

3. Elimination of the spatial and temporal dependence

To gauge away the spatial and temporal dependence in the atom-light interaction operators $\hat{H}'_{\text{intra}}$ and $\hat{H}'_{\text{inter}}$, a fast oscillating (both spatially and temporarily) phase is factored out from each operator $\hat{\Phi}_{j\gamma}(\mathbf{r}_\perp)$ by writing

$$\begin{pmatrix} \hat{\Phi}_{\uparrow 1}(\mathbf{r}_\perp) \\ \hat{\Phi}_{\downarrow 1}(\mathbf{r}_\perp) \\ \hat{\Phi}_{\uparrow 2}(\mathbf{r}_\perp) \\ \hat{\Phi}_{\downarrow 2}(\mathbf{r}_\perp) \end{pmatrix} = \begin{pmatrix} \hat{\psi}_{\uparrow 1}(\mathbf{r}_\perp)e^{-i\kappa y - i\epsilon_{1\uparrow}t} \\ \hat{\psi}_{\downarrow 1}(\mathbf{r}_\perp)e^{-i\kappa x - i\epsilon_{1\downarrow}t} \\ \hat{\psi}_{\uparrow 2}(\mathbf{r}_\perp)e^{i\kappa x - i\epsilon_{2\uparrow}t} \\ \hat{\psi}_{\downarrow 2}(\mathbf{r}_\perp)e^{i\kappa y - i\epsilon_{2\downarrow}t} \end{pmatrix}. \tag{A4}$$

Applying the rotating wave approximation, the resultant time- and position-independent single-particle Hamiltonian is given by Eqs. (2)–(5) in the main text. Note that the gauge transformation (A4) introduces an additional SOC term $\hat{H}_{\text{SOC}}$ given by Eq. (5).

Appendix B: Eigenvalue problem and Hamiltonian in rotated basis

1. The single-particle Hamiltonian and its eigenstates

Denoting

$$|\uparrow, 1\rangle = \begin{pmatrix} 1 \\ 0 \\ 0 \\ 0 \end{pmatrix}, \quad |\downarrow, 1\rangle = \begin{pmatrix} 0 \\ 1 \\ 0 \\ 0 \end{pmatrix}, \tag{B1}$$

$$|\uparrow, 2\rangle = \begin{pmatrix} 0 \\ 0 \\ 1 \\ 0 \end{pmatrix}, \quad |\downarrow, 2\rangle = \begin{pmatrix} 0 \\ 0 \\ 0 \\ 1 \end{pmatrix},$$

the single-particle Hamiltonian, Eqs. (1)–(4), can be expressed in the momentum space as:

$$H_0 = \frac{\hbar^2}{2m}(k^2 + \kappa^2) + H_{\text{SOC},\mathbf{k}}\,, \tag{B2}$$

where

$$H_{\text{SOC},\mathbf{k}} = \frac{\hbar^2}{m}\mathbf{k}\cdot\mathbf{q} + H_{\text{inter}} + H_{\text{intra}}\,, \tag{B3}$$

and

$$\mathbf{q} = \kappa\mathbf{e}_x(|\uparrow, 2\rangle\langle\uparrow, 2| - |\downarrow, 1\rangle\langle\downarrow, 1|) + \kappa\mathbf{e}_y(|\downarrow, 2\rangle\langle\downarrow, 2| - |\uparrow, 1\rangle\langle\uparrow, 1|)\,, \tag{B4}$$

$$H_{\text{inter}} = J(|\uparrow, 2\rangle\langle\uparrow, 1| + |\downarrow, 2\rangle\langle\downarrow, 1|) + \text{H.c.}\,, \tag{B5}$$

$$H_{\text{intra}} = \Omega\left(e^{i\varphi}|\uparrow, 1\rangle\langle\downarrow, 1| + e^{-i\varphi}|\uparrow, 2\rangle\langle\downarrow, 2|\right) + \text{H.c.}\,. \tag{B6}$$

where the momentum $\mathbf{k} \equiv \mathbf{k}_\perp = (k_x, k_y)$ is in the xy plane.

The Hamiltonian $H_{\mathrm{SOC},\mathbf{k}}$ can be represented in a block diagonal form:

$$H_{\mathrm{SOC},\mathbf{k}} = \begin{pmatrix} h_{1,\mathbf{k}} & J \\ J & h_{2,\mathbf{k}} \end{pmatrix} \tag{B7}$$

with

$$h_{1,\mathbf{k}} = \begin{pmatrix} -2k_y & \Omega e^{i\varphi} \\ \Omega e^{-i\varphi} & -2k_x \end{pmatrix}, \quad h_{2,\mathbf{k}} = \begin{pmatrix} 2k_x & \Omega e^{-i\varphi} \\ \Omega e^{i\varphi} & 2k_y \end{pmatrix}, \tag{B8}$$

and the off-diagonal 2×2 blocks $J \equiv JI$ being proportional to the 2×2 unit matrix I. The block diagonal form of the Hamiltonian H_0 given by Eqs. (B2), (B7) and (B8), allows to find its eigenstates in a straightforward way:

$$E_{\alpha,\eta} = 1 + k^2 + \alpha \sqrt{\Omega^2 + J^2 + 2k^2 + 2\eta a_{\mathbf{k}}}, \tag{B9}$$

with $\alpha = \pm 1$, $\eta = \pm 1$, where the energy is measured in the units of the of the recoil energy $E_{\mathrm{rec}} = \hbar^2\kappa^2/2m$, whereas the momentum is measured in terms of the recoil momentum κ. Here

$$a_{\mathbf{k}} = \sqrt{\Omega^2(k_x + k_y)^2 + J^2(k_x - k_y)^2 + (k_x^2 - k_y^2)^2}, \tag{B10}$$

with $\mathbf{k} = k(\cos\phi\, \mathbf{e}_x + \sin\phi\, \mathbf{e}_y)/2$, and ϕ being an azimuthal angle in the momentum space. The lowest dispersion branch

$$E_g = E_{-1,1} = 1 + k^2 - \sqrt{\Omega^2 + J^2 + 2k^2 + 2a_{\mathbf{k}}}, \tag{B11}$$

is obtained by taking $\alpha = -1$, $\eta = +1$. For $\Omega^2 = J^2 \gg E_{\mathrm{rec}}^2$ the eigenvector corresponding to the lowest dispersion branch is given by Eq. (11) of the main text:

$$\chi = \begin{pmatrix} \sqrt{2}\cos\phi \\ i(1 - \sin\phi + \cos\phi) \\ 1 - \sin\phi - \cos\phi \\ -\sqrt{2}i(1 - \sin\phi) \end{pmatrix} \frac{e^{i\mathbf{k}\cdot\mathbf{r}_\perp}}{\sqrt{8 - 8\sin\phi}}. \tag{B12}$$

To gain more insight into the interaction-induced symmetry breaking, we will present the Hamiltonian in terms of the basis vectors for which the atoms possess the minimum interaction energy on the Rashba ring. The projection of such a Hamiltonian to lower energy states gives rise to the appearance of Rashba Hamiltonian. These issues will be addressed next.

2. Hamiltonian in rotated basis and reduction to the Rashba Hamiltonian

In Sec. III C of the main text, the variational approach shows that the minimization of interaction energy breaks the rotational symmetry of the Rashba ring. In the case of single momentum states (PW-II phase), the interaction energy between the atoms acquires a minimum value for $\phi = 3\pi/4$ or $\phi = -\pi/4$, i.e. for $\mathbf{k}$ and $-\mathbf{k}$ along a diagonal $\mathbf{e}_x - \mathbf{e}_y$. For these azimuthal angles the spinor part of eigenvectors $\chi^{(1)} = \chi(3\pi/4)$ and $\chi^{(2)} = \chi(-\pi/4)$ read using Eq.(B12) or Eq. (11) in the main text:

$$\chi^{(1)} = \frac{1}{b_-}\begin{pmatrix} -1 \\ ia_- \\ 1 \\ ia_- \end{pmatrix}, \qquad \chi^{(2)} = \frac{1}{b_+}\begin{pmatrix} 1 \\ ia_+ \\ 1 \\ -ia_+ \end{pmatrix}, \tag{B13}$$

where

$$b_\pm = 2\sqrt{2 \pm \sqrt{2}}, \qquad a_\pm = 1 \pm \sqrt{2}.$$

The vectors $\chi^{(1)}$ and $\chi^{(2)}$ can serve as a basis for the lowest dispersion branch. To have a complete rotated bases, we choose the remaining two orthogonal vectors to be

$$\chi^{(3)} = \frac{1}{b_-}\begin{pmatrix} -1 \\ i \\ a_- \\ -ia_- \end{pmatrix}, \qquad \chi^{(4)} = \frac{1}{b_+}\begin{pmatrix} 1 \\ i \\ a_+ \\ ia_+ \end{pmatrix}. \tag{B14}$$

In the rotated basis, the Hamiltonian $H_{\mathrm{SOC},\mathbf{k}}$, Eq. (B7), reads for $\Omega = J$

$$H_{\mathrm{SOC},\mathbf{k}} = \begin{pmatrix} -\sqrt{2}\Omega & 0 \\ 0 & \sqrt{2}\Omega \end{pmatrix} + \begin{pmatrix} \frac{1}{\sqrt{2}}(k_-\sigma_z + k_+\sigma_x) & -k_y I + ik_x\sigma_y \\ -k_y I - ik_x\sigma_y & -\frac{1}{\sqrt{2}}(k_-\sigma_x + k_+\sigma_z) \end{pmatrix}, \tag{B15}$$

with $k_\pm = k_x \pm k_y$.

For $\Omega^2 = J^2 \gg E_{\mathrm{rec}}^2$, the upper and lower pairs states are separated by the energy $\approx 2\sqrt{2}\Omega$. In that case one can neglect the coupling between the lower and upper two pairs of states. The Hamiltonian projected onto the manifold of low-energy states $\chi^{(1)}$ and $\chi^{(2)}$ reduces to the usual Rashba-type Hamiltonian

$$H_{\mathrm{SOC},\mathbf{k}} \to \frac{1}{\sqrt{2}}(k_-\sigma_z + k_+\sigma_x). \tag{B16}$$

subject to the rotation of the spin by $\pi/2$ along the x axis transforming σ_z to σ_y.

3. Interaction energy

According to the interaction Hamiltonian (12), the contact interaction between atoms is described by the functional

$$E_{\mathrm{int}} = \sum_{j=1}^{2} \int d^2\mathbf{r} \left(\frac{g_\uparrow}{2}|\psi_{\uparrow,j}|^4 + \frac{g_\downarrow}{2}|\psi_{\downarrow,j}|^4 + g_{\uparrow\downarrow}|\psi_{\uparrow,j}|^2|\psi_{\downarrow,j}|^2 \right). \tag{B17}$$

Let us assume that the state of the atomic cloud is a superposition of lowest states $\chi^{(1)}$ and $\chi^{(2)}$ with the coefficients $\tilde{\psi}_1$ and $\tilde{\psi}_2$:

$$\chi = \chi^{(1)}\tilde{\psi}_1 + \chi^{(2)}\tilde{\psi}_2 \tag{B18}$$

For $g_\uparrow = g_\downarrow$, the interaction energy (B17) becomes

$$E_{\rm int} = \frac{1}{16}\Big[(3g_\uparrow + g_{\uparrow\downarrow})(|\tilde{\psi}_1|^4 + |\tilde{\psi}_2|^4) + 4(g_\uparrow + 2g_{\uparrow\downarrow})|\tilde{\psi}_1|^2|\tilde{\psi}_2|^2 + (g_\uparrow + g_{\uparrow\downarrow})\left(\tilde{\psi}_1^{*2}\tilde{\psi}_2^2 + \tilde{\psi}_2^{*2}\tilde{\psi}_1^2\right)\Big]. \quad \text{(B19)}$$

Taking $\tilde{\psi}_1 = -\psi\sin(\frac{1}{2}(\phi+\frac{\pi}{4}))$, $\tilde{\psi}_2 = \psi\cos(\frac{1}{2}(\phi+\frac{\pi}{4}))$ the superposition vector (B18) reduces to Eq.(B12) or Eq. (11) in the main text. For $\phi = -\pi/4$, one has $\tilde{\psi}_1 = 0$, so there is only one column $\chi^{(2)}$. Thus ϕ indeed represents the azimuthal angle in the momentum space. Inserting the expressions for $\tilde{\psi}_1$ and $\tilde{\psi}_2$ into Eq. (B19) we get

$$E_{\rm int} = \frac{c_0}{8} + \frac{c_0}{32}(1+\sin 2\phi) + \frac{c_2}{32}(1-\sin 2\phi) \quad \text{(B20)}$$

where we assume $g_\uparrow = g_\downarrow = g$ and introduce $c_0 = g + g_{\uparrow\downarrow}$ and $c_2 = g - g_{\uparrow\downarrow}$, with $c_0 \gg c_2$. This is equivalent to the expression (21) of the main text for the PW-II phase. Using the projected basis χ_1 and χ_2, the interaction energy $E_{\rm int}$ given by Eq. (B20) acquires a minimum value for $\phi = 3\pi/4$ or $\phi = -\pi/4$, as required. Thus the interaction appears to be highly anisotropic along the Rashba ring.

[1] Y.-J. Lin, R. L. Compton, K. Jiménez-García, J. V. Porto, and I. B. Spielman, Nature (London) **462**, 628 (2009).
[2] J. Struck, C. Ölschläger, M. Weinberg, P. Hauke, J. Simonet, A. Eckardt, M. Lewenstein, K. Sengstock, and P. Windpassinger, Phys. Rev. Lett. **108**, 225304 (2012).
[3] M. Aidelsburger, M. Atala, M. Lohse, J. T. Barreiro, B. Paredes, and I. Bloch, Physical Review Letters **111**, 185301 (2013).
[4] H. Miyake, G. A. Siviloglou, C. J. Kennedy, W. C. Burton, and W. Ketterle, Phys. Rev. Lett. **111**, 185302 (2013).
[5] G. Jotzu, M. Messer, R. Desbuquois, M. Lebrat, T. Uehlinger, D. Greif, and T. Esslinger, Nature **515**, 237 (2014).
[6] R. Dum and M. Olshanii, Phys. Rev. Lett. **76**, 1788 (1996).
[7] P. M. Visser and G. Nienhuis, Phys. Rev. A **57**, 4581 (1998).
[8] G. Juzeliūnas and P. Öhberg, Phys. Rev. Lett. **93**, 033602 (2004).
[9] G. Juzeliūnas, J. Ruseckas, P. Öhberg, and M. Fleischhauer, Phys. Rev. A **73**, 025602 (2006).
[10] J. Dalibard, F. Gerbier, G. Juzeliūnas, and P. Öhberg, Rev. Mod. Phys. **83**, 1523 (2011).
[11] N. Goldman, G. Juzeliūnas, P. Öhberg, and I. B. Spielman, Rep. Progr. Phys. **77**, 126401 (2014).
[12] M. Lewenstein, S. Anna, and A. Verònica, *Ultracold Atoms in Optical Lattices: Simulating quantum many-body systems* (Oxford University Press, 2012).
[13] J. Ruseckas, G. Juzeliūnas, P. Öhberg, and M. Fleischhauer, Phys. Rev. Lett. **95**, 010404 (2005).
[14] H. Zhai, Rep. Prog. Phys. **78**, 026001 (2015).
[15] C. Wang, C. Gao, C.-M. Jian, and H. Zhai, Phys. Rev. Lett. **105**, 160403 (2010).
[16] Z. F. Xu, R. Lü, and L. You, Phys. Rev. A **83**, 053602 (2011).
[17] C.-F. Liu and W. M. Liu, Phys. Rev. A **86**, 033602 (2012).
[18] J. Radić, T. A. Sedrakyan, I. B. Spielman, and V. Galitski, Phys. Rev. A **84**, 063604 (2011).
[19] X.-F. Zhou, J. Zhou, and C. Wu, Phys. Rev. A **84**, 063624 (2011).
[20] S. Sinha, R. Nath, and L. Santos, Phys. Rev. Lett. **107**, 270401 (2011).
[21] T. Ozawa and G. Baym, Phys. Rev. A **85**, 013612 (2012).
[22] T. Ozawa and G. Baym, Phys. Rev. A **85**, 063623 (2012).
[23] C.-F. Liu, Y.-M. Yu, S.-C. Gou, and W.-M. Liu, Phys. Rev. A **87**, 063630 (2013).
[24] X. Chen, M. Rabinovic, B. M. Anderson, and L. Santos, Phys. Rev. A **90**, 043632 (2014).
[25] W. Han, G. Juzeliūnas, W. Zhang, and W.-M. Liu, Phys. Rev. A **91**, 013607 (2015).
[26] S.-W. Su, S.-C. Gou, I.-K. Liu, I. B. Spielman, L. Santos, A. Acus, A. Mekys, J. Ruseckas, and G. Juzeliūnas, New J. Phys. **17**, 033045 (2015).
[27] L. Jiang, X.-J. Liu, H. Hu, and H. Pu, Phys. Rev. A **84**, 063618 (2011).
[28] J. P. Vyasanakere and V. B. Shenoy, New J. Phys. **14**, 043041 (2012).
[29] J. Zhou, W. Zhang, and W. Yi, Phys. Rev. A **84**, 063603 (2011).
[30] X.-J. Liu and H. Hu, Phys. Rev. A **85**, 033622 (2012).
[31] X.-J. Liu and H. Hu, Phys. Rev. A **88**, 023622 (2013).
[32] Z. Cai, X. Zhou, and C. Wu, Phys. Rev. A **85**, 061605(R) (2012).
[33] J. Radić, A. DiCiolo, K. Sun, and V. Galitski, Phys. Rev. Lett. **109**, 085303 (2012).
[34] W. S. Cole, S. Zhang, A. Paramekanti, and N. Trivedi, Phys. Rev. Lett. **109**, 085302 (2012).
[35] Z. Xu, W. S. Cole, and S. Zhang, Phys. Rev. A **89**, 051604(R) (2014).
[36] Z. Chen and Z. Liang, Phys. Rev. A **93**, 013601 (2016).
[37] Y.-J. Lin, K. Jiménez-García, and I. B. Spielman, Nature **471**, 83 (2011).
[38] J.-Y. Zhang, S.-C. Ji, Z. Chen, L. Zhang, Z.-D. Du, B. Yan, G.-S. Pan, B. Zhao, Y.-J. Deng, H. Zhai, S. Chen, and J.-W. Pan, Phys. Rev. Lett. **109**, 115301 (2012).
[39] P. Wang, Z.-Q. Yu, Z. Fu, J. Miao, L. Huang, S. Chai, H. Zhai, and J. Zhang, Phys. Rev. Lett. **109**, 095301 (2012).
[40] L. W. Cheuk, A. T. Sommer, Z. Hadzibabic, T. Yefsah, W. S. Bakr, and M. W. Zwierlein, Phys. Rev. Lett. **109**, 095302 (2012).
[41] R. A. Williams, L. J. LeBlanc, K. Jiménez-García, M. C. Beeler, A. R. Perry, W. D. Phillips, and I. B. Spielman, Science **335**, 314 (2012).
[42] L. J. LeBlanc, M. C. Beeler, K. Jimenez-Garcia, A. R. Perry, S. Sugawa, R. A. Williams, and I. B. Spielman, New. J. Phys. **15**, 073011 (2013).
[43] C. Qu, C. Hamner, M. Gong, C. Zhang, and P. Engels, Phys. Rev. A **88**, 021604(R) (2013).
[44] Z. Fu, L. Huang, Z. Meng, P. Wang, L. Zhang, S. Zhang, H. Zhai, P. Zhang, and J. Zhang, Nature Phys. **10**, 815 (2014).
[45] X.-J. Liu, M. F. Borunda, X. Liu, and J. Sinova, Phys. Rev. Lett. **102**, 046402 (2009).
[46] Y. Li, L. P. Pitaevskii, and S. Stringari, Phys. Rev. Lett. **108**, 225301 (2012).
[47] Y. Li, G. I. Martone, L. P. Pitaevskii, and S. Stringari, Phys. Rev. Lett. **110**, 235302 (2013).
[48] T. D. Stanescu, C. Zhang, and V. Galitski, Phys. Rev. Lett. **99**, 110403 (2007).
[49] A. Jacob, P. Öhberg, G. Juzeliūnas, and L. Santos, Appl. Phys. B **89**, 439 (2007).

[50] T. D. Stanescu, B. Anderson, and V. Galitski, Phys. Rev. A **78**, 023616 (2008).
[51] G. Juzeliūnas, J. Ruseckas, M. Lindberg, L. Santos, and P. Öhberg, Phys. Rev. A **77**, 011802(R) (2008).
[52] C. Zhang, Phys. Rev. A **82**, 021607(R) (2010).
[53] D. L. Campbell, G. Juzeliūnas, and I. B. Spielman, Phys. Rev. A **84**, 025602 (2011).
[54] S.-W. Su, I.-K. Liu, Y.-C. Tsai, W.-M. Liu, and S.-C. Gou, Phys. Rev. A **86**, 023601 (2012).
[55] B. M. Anderson, G. Juzeliūnas, V. M. Galitski, and I. B. Spielman, Phys. Rev. Lett. **108**, 235301 (2012).
[56] Z.-F. Xu, L. You, and M. Ueda, Phys. Rev. A **87**, 063634 (2013).
[57] B. M. Anderson, I. B. Spielman, and G. Juzeliūnas, Phys. Rev. Lett. **111**, 125301 (2013).
[58] Q. Sun, L. Wen, W.-M. Liu, G. Juzeliūnas, and A.-C. Ji, Phys. Rev. A **91**, 033619 (2015).
[59] L. Huang, Z. Meng, P. Wang, P. Peng, S.-L. Zhang, L. Chen, D. Li, Q. Zhou, and J. Zhang, Nature Phys. **doi:10.1038/nphys3672** (2016).
[60] Z. Meng, L. Huang, P. Peng, D. Li, L. Chen, Y. Xu, C. Zhang, P. Wang, and J. Zhang, arXiv:1511.08492 (2015).
[61] Two dimensional spin-orbit coupling has also been recently realized using another approach which relies on optical lattices, see Z. Wu, L. Zhang, W. Sun, X.-T. Xu, B.-Z. Wang, S.-C. Ji, Y. Deng, S. Chen, X.-J. Liu and J.-W. Pan, arXiv:1511.08170.
[62] W. Hung, P. Huang, F.-C. Wu, M. Bruvelis, H.-Y. Xiao, A. Ekers, and I. A. Yu, J. Opt. Soc. Am. B **32**, B32 (2015).
[63] J. Sebby-Strabley, M. Anderlini, P. S. Jessen, and J. V. Porto, Phys. Rev. A **73**, 033605 (2006).
[64] K. Kasamatsu, M. Tsubota, and M. Ueda, Phys. Rev. A **71**, 043611 (2005).
[65] S. A. Chin and E. Krotscheck, Phys. Rev. E **72**, 036705 (2005).
[66] N. D. Mermin and T.-L. Ho, Phys. Rev. Lett. **36**, 594 (1976).
[67] T. Mizushima, K. Machida, and T. Kita, Phys. Rev. Lett. **89**, 030401 (2002).
[68] T.-L. Ho, Phys. Rev. Lett. **81**, 742 (1998).
[69] T. Ohmi and K. Machida, J. Phys. Soc. Jpn. **67**, 1822 (1998).
[70] I. H. Deutsch and P. S. Jessen, Phys. Rev. A **57**, 1972 (1998).